Composite Adaptive Synchronous Control of Dual-Drive Gantry Stage With Load Movement

PENGWEI SHI [1], **XINGHU YU** [3], **XUEBO YANG** [1] **(Member, IEEE),**
JUAN J. RODRÍGUEZ-ANDINA [4] **(Fellow, IEEE), WEICHAO SUN** [1] **(Senior Member, IEEE),**
AND HUIJUN GAO [1,2] **(Fellow, IEEE)**

[1] Research Institute of Intelligent Control and Systems, Harbin Institution of Technology, Harbin 150001, China
[2] Research Center of Intelligent Control and Systems, Yongjiang Laboratory, Ningbo 315200, China
[3] Ningbo Institute of Intelligent Equipment Technology Company Ltd., Ningbo 315200, China
[4] Department of Electronic Technology, University of Vigo, 36310 Vigo, Spain

CORRESPONDING AUTHORS: **WEICHAO SUN; HUIJUN GAO** (e-mail: w.sun@hit.edu.cn; hjgao@hit.edu.cn).

ABSTRACT In gantry systems, load usually moves according to different production tasks. The continuous change of the beam centroid position is a non-negligible factor for achieving high-performance synchronous control. Therefore, it cannot be simply treated as an external disturbance. In addition, advanced controller design and model parameter identification are very important for precision motion control systems. This article addresses the synchronous control of dual-drive gantry platforms with load movement to improve their steady-state and transient performance. Based on the analysis of the rigid and flexible characteristics of gantry mechanical components, a rigid-flexible coupling dynamic model is proposed, which provides a theoretical basis for the control system design. To ensure zero steady-state tracking error and parameter convergence in the presence of parameter uncertainties and unknown disturbances, a composite adaptive control method integrating excellent output tracking performance and parameter estimation is presented. Furthermore, the bridge between load movement and centroid position is established through frequency domain identification, which facilitates reasonable thrust distribution. Comparative experimental results are presented that confirm the effectiveness and advantages of the proposed synchronous control scheme.

INDEX TERMS Composite adaptive algorithm, load movement, synchronization control, system identification.

I. INTRODUCTION

Modern industry is constantly moving toward refinement, efficiency, and intelligence, which also requires continuously improving performance of production and processing equipment. In recent years, dual-drive gantry stages have attracted much attention as the core component of the new generation of high-end equipment, in fields, such as semiconductor production, electronic assembly, digital printing, or biomedicine, and has set off a research upsurge from industrial scholars [1], [2], [3], [4], [5], [6], [7]. Different from the cooperation between traditional rotary motors and ball screws, the essential advantage of dual-drive gantry stages lies in their unique structural characteristics and the joint driving method of dual linear motors, which allows systems to obtain large thrust while avoiding the energy loss caused by the wear of mechanical transmission. However, coupling constraints between redundant axes and complex industrial environments make it extremely difficult to accurately determine the dynamic model of the system. Unavoidable parameter uncertainties and unknown nonlinearities (such as ripple force, nonlinear electromagnetic force, friction model uncertainties, or external random disturbances [8], [9], [10], [11], [12], [13]) in the dual-drive gantry system also bring serious challenges to actual production control. In particular, the accuracy of

synchronous tracking directly affects processing quality and production efficiency of products. In addition, the robustness and transient steady-state performance of gantry systems are also factors that must be considered in the design of the corresponding controllers.

In order to overcome the aforementioned difficulties, many control algorithms, such as sliding-mode control (SMC), adaptive control, iterative learning, artificial neural network, or observer control, have been applied and achieved good results [14], [15], [16], [17], [18]. Dong et al. [19] studied the fast positioning and tracking problem of single-axis gantry, and proposed a global nonsingular SMC law by combining the natural logarithm function, which make the system achieve better accuracy and fast convergence. In order to effectively deal with disturbance problems in periodic tasks of linear motors, an intelligent observer control method based on wavelet neural network is proposed in [20], achieving the good tracking and robust performance. Kira et al. [21] extended the single-axis iterative learning algorithm and proposed a contour controller design based on the cross-coupling control scheme to improve motion control accuracy of the whole gantry system. In order to overcome problems related to parameter uncertainties and nonlinear disturbances, an adaptive robust control (ARC) algorithm [22], [23] integrating parameter adaptation rate and robust control law is proposed and widely used in mechatronics systems. The direct ARC algorithm has significant advantages in reducing the output tracking error, but the estimation of the system parameters is only guaranteed to be bounded and cannot converge to the real value. The indirect ARC algorithm aims to reduce parameter estimation error, but the transient response of the resulting system is poor due to the lack of fast model compensation, and its stability is very conservative. Therefore, a composite adaptive control algorithm is proposed in this article to ensure that the system has zero steady-state tracking error and parameter convergence characteristics in the presence of parameter uncertainties and nonlinear disturbances.

Synchronous control with coupling effects is particularly complex and has received significant attention from researchers [24], [25], [26], [27]. The upper limit for the performance of gantry stages often depends on the accuracy of system's model and control. Different from the previous fully rigid model assumption of dual-drive gantry systems, Chen et al. [28] considered the flexible characteristics of ball bearings at the linear guide. Combined with the frequency domain response curve, the existence of non-negligible high-frequency flexible dynamics was noted, and a more reasonable second-order rigid-flexible coupling model was derived. Li et al. [29] also analyzed the flexible characteristics of the gantry crossbeam subsystem, and realized the thrust distribution of the two driving shafts with ARC algorithm, so that good synchronization performance was achieved in terms of steady-state accuracy. Li et al. [30] used an online parameter estimation algorithm to predict the centroid of the beam under static load, and thereby improve the steady-state and transient performance of the system. In spite of the importance
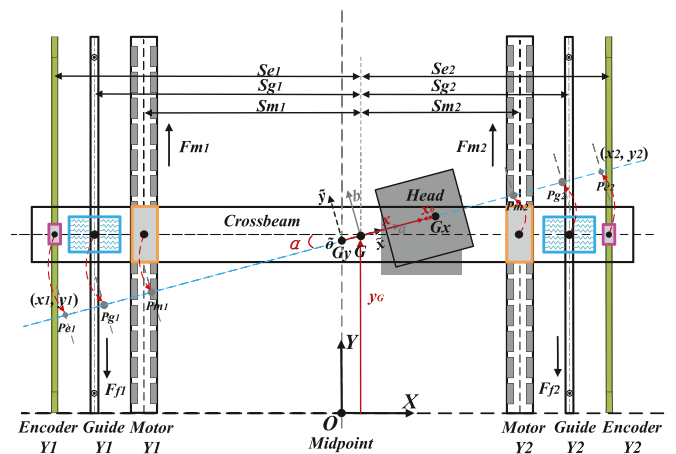

FIGURE 1. Dual-drive gantry stage with load movement.

of the topic, the impact of load motion on the system as an external disturbance is usually not considered by researchers. However, the change of the beam centroid position caused by the load is indeed a non-negligible factor and an urgent problem to be solved for precision synchronous control. The relationship between the rotation center of mass and load motion is defined in the form of a function in [31], but the method of thrust distribution there sacrifices the transient performance of the system.

Based on the analysis mentioned above, the main contributions and challenges of this article are as follows.

1) Fully considering the kinematic characteristics of the gantry system, the establishment of a coupled dynamic model is the primary task.
2) Design an excellent controller to effectively deal with parameter uncertainties and unknown nonlinear disturbances in the system.
3) The relationship between the load movement and the center of mass of the beam is established to further improve the synchronization control accuracy.

The rest of this article is organized as follows. In Section II, the coupling dynamic model of the gantry subsystem is defined and the input/output transfer function is derived. The design of the proposed composite adaptive controller is presented in Section III. In Section IV, the dynamic relationship between centroid position and load is determined by frequency domain identification. Comparative experiments to validate the proposed control method are presented and discussed in Section V. Finally, Section VI concludes this article.

II. PROBLEM FORMULATION
A. KINEMATIC DESCRIPTION
A dual-drive gantry stage with load movement is represented in Fig. 1. The mechanical beam, including linear motor (orange), rigidly connected slider (blue), and reading head of grating ruler (magenta), is fixed at both ends of the gantry stage.

Ignoring the small lateral deviation of the beam during rotation, the generalized coordinates **OXY** and the rotating coordinates **Gab** are defined, respectively. õx̃ỹ represents the mapping of *OXY* on Gab. Without loss of generality, the centroid positions of mechanical beam and moving head (including the payload) are respectively expressed as **Gy** and **Gx**, whereas the equivalent centroid positions of the whole beam (including mechanical beam and moving head) are expressed as **G**, and their positions change with load movement. **x** represents the displacement of the grating encoder, and **x₀** is the offset of the centroid of the moving head caused by uneven load distribution or encoder installation error. When the beam rotates, it intersects the grating ruler, linear guide, and linear motor at P_{ei}, P_{gi}, and P_{mi}, respectively, and their nominal span values can be obtained by either consulting the technical manual or through measurements. The position coordinates of the two ends of the beam are denoted by $(x1, y1)$ and $(x2, y2)$, respectively. Obviously, according to the position coordinates y_i obtained by the grating encoder ($i = 1, 2$, and $y_i = y_{ei}$), the geometric relationship y_i and rotation α ($\alpha \approx 0$) can be expressed as

$$y_{\star 1} = y_G - S_{\star 1}\sin(\alpha) \approx y_G - S_{\star 1}\alpha$$

$$y_{\star 2} = y_G + S_{\star 2}\sin(\alpha) \approx y_G + S_{\star 2}\alpha$$

$$\alpha \approx \sin(\alpha) = (y_2 - y_1)/S_e \quad (1)$$

where $\star$ represent the characters e, g, and m, respectively. $S_e = S_{e1} + S_{e2}$ is the distance between two parallel grating rulers along the Y-axis.

B. DYNAMIC REPRESENTATION

This article focuses on the synchronous control of the gantry system with load movement, without involving the dynamic modeling of the moving head. Ignoring other unknown disturbances for the moment, the system is affected by electromagnetic driving force F_{mi} and friction force F_{fi}. The servo driver with current loop feedback control has high internal bandwidth and large gain, so the electrical dynamics can be ignored. The driving force model of the motor can be described as $F_{mi} = K_i U_i$. K_i represents the driving thrust coefficient of the motor, and U_i its the control input voltage. The construction of an accurate friction model is a complex task, for which the popular Lugre model with rich friction phenomena can be used, expressed as [11]

$$F_f(\dot{y}_i) = \left[F_c + (F_s - F_c)e^{-\left(\frac{\dot{y}_i}{y_s}\right)^{\delta}}\right]\text{sgn}(\dot{y}_i) + \gamma\dot{y}_i \quad (2)$$

where F_c is the Coulomb friction force, F_s the maximum static friction, and y_i and y_s the motor feedback speed and critical Stribeck speed, respectively. γ is the viscous friction coefficient, and δ an empirical design parameter.

Noting the presence of the sign function in the first term on the right side of the equation, the discontinuity of the model at zero velocity excites the high-frequency dynamics of the system. In practice, continuous or sufficiently smooth functions, such as $S_f(\dot{y}) = \arctan(500\dot{y})$, are used as approximations.

Therefore, the friction model can be rewritten as

$$F_f(\dot{y}_i) = B_i\dot{y}_i + A_i S_f(\dot{y}_i) \quad i = 1, 2 \quad (3)$$

where B_i and A_i represent viscous friction and Coulomb friction coefficient, respectively. The ball support is squeezed and deformed when the crossbeam rotates, and the equivalent work generated at the guide rail can be expressed as [26]

$$W_{Ri} = K_a\alpha \quad (4)$$

where K_a represents the equivalent rotational stiffness, which reflects the relationship between rotation angle and constrained internal force.

For the sake of simplicity, let us define the following mathematical symbols: $\bullet k$ represents the dimensionally simplified value of relative motor thrust coefficient K_1 (i.e., $\bullet k = \bullet/K_1$); $\bar{\bullet}$ and $\check{\bullet}$ are the constant and time-varying components of $\bullet$, respectively; $\hat{\bullet}$ and $\tilde{\bullet}$ denote the estimated value and estimation error of parameter $\bullet$ (i.e., $\tilde{\bullet} = \hat{\bullet} - \bullet$); the low- and high-frequency components of signal $\bullet$ are defined as $\bullet_*$ and $\bullet^*$, respectively; $\bullet_{min}$ and $\bullet_{max}$ stand for the minimum and maximum values of parameter $\bullet$; signal $\bullet$ is expressed as $\bullet_f$ after filtering function processing and $\sigma(\bullet)$ is the eigenvalue of $\bullet$.

Using Newton's second law, the coupling dynamic model of the dual-drive gantry stage system can be expressed as

$$M_k\ddot{y}_G = u_1 + K_m u_2 - B_{fk}\dot{y}_G + B_{gk}\dot{\alpha} - A_{fk}S_f(\dot{y}_G) + d_{yk}$$

$$J_k\ddot{\alpha} = -S_{m1}u_1 + K_m S_{m2}u_2 - B_{sk}\dot{\alpha} - K_{ak}\alpha + B_{gk}\dot{y}_G$$

$$+ A_{gk}S_f(\dot{y}_G) + d_{\alpha k} \quad (5)$$

where $K_m = K_2/K_1$; M_k and J_k represent the inertial mass and rotational inertia of the whole beam, respectively. In addition, $A_{fk} = A_{1k} + A_{2k}$, $A_{gk} = A_{1k}S_{g1} - A_{2k}S_{g2}$, $B_{fk} = B_{1k} + B_{2k}$, $B_{gk} = B_{1k}S_{g1} - B_{2k}S_{g2}$, $B_{sk} = B_{1k}S_{g1}^2 + B_{2k}S_{g2}^2$. $d_{yk} = \bar{d}_{yk} + \check{d}_{yk}$ and $d_{\alpha k} = \bar{d}_{\alpha k} + \check{d}_{\alpha k}$ represent various uncertainties and contain modeling approximation errors $A_{fk}S_f(\dot{y}_G) - A_{ik}S_f(\dot{y}_i)$ and $A_{gk}S_f(\dot{y}_G) - (-1)^{i-1}A_{ik}S_f(\dot{y}_i)S_{gi}$, respectively.

To analyze the control input (U_i) / output (y_G) dynamic response of the system, ignoring the Coulomb friction term and various uncertainties, the Laplace transform of (5) can be obtained as

$$P_1(s) = \frac{1}{M_k s^2 + B_{fk}s}\frac{J_k s^2 + [B_{sk} - B_{gk}S_{m1}]s + K_{ak}}{J_k s^2 + B_{sk}s + K_{ak}}$$

$$P_2(s) = \frac{k_m}{M_k s^2 + B_{fk}s}\frac{J_k s^2 + [B_{sk} + B_{gk}S_{m2}]s + K_{ak}}{J_k s^2 + B_{sk}s + K_{ak}}. \quad (6)$$

Note that B_{gk}^2 is omitted because $K_{ak}M_k + B_{fk}B_{sk} \gg B_{gk}^2$. Furthermore, the expression in (1) is introduced into (6), which allows (6) to be rewritten as ($U_i \rightarrow y_1$)

$$P_1'(s) = \frac{1}{M_k s^2 + B_{fk}s}\frac{(J_k + M_k S_{e1}S_{m1})s^2 + C_1 s + K_{ak}}{J_k s^2 + B_{sk}s + K_{ak}}$$

$$P_2'(s) = \frac{k_m}{M_k s^2 + B_{fk}s}\frac{(J_k - M_k S_{e1}S_{m2})s^2 + C_2 s + K_{ak}}{J_k s^2 + B_{sk}s + K_{ak}} \quad (7)$$
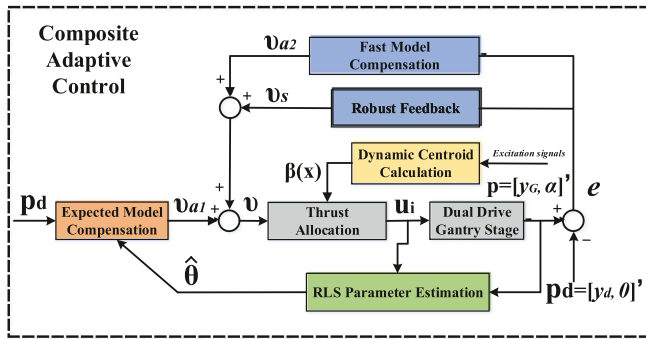
FIGURE 2. Block diagram of the proposed composite adaptive synchronous control.

where $C_1 = B_{sk} - B_{gk}S_{e1} - B_{gk}S_{m1} + B_{fk}S_{e1}S_{m1}$ and $C_2 = B_{sk} - B_{gk}S_{e1} - B_{fk}S_{e1}S_{m2} + B_{gk}S_{m2}$. The first-order inertia link corresponds to the low-frequency rigid dynamics of the system, whereas the high-order transfer function form with zero poles represents the high-frequency flexible dynamics.

Defining the normalized matrix vector $p = [y_G(t), \alpha(t)]^T$, the dynamic equation (5) of the dual-drive gantry stage in the generalized coordinate system can be rewritten as

$$M_p \ddot{p} + B_p \dot{p} + K_p p + A_p S_f(\dot{p}) = \upsilon + \bar{d}_p + \check{d}_p \qquad (8)$$

where $\dot{p} = [\dot{y}_G(t), \dot{\alpha}(t)]^T$ and $\ddot{p} = [\ddot{y}_G(t), \ddot{\alpha}(t)]^T$ are the velocity and acceleration vector matrices, respectively, and $\upsilon = \kappa[u_1, u_2]^T$ is a virtual control input with $\kappa = [1, K_m; -S_{m1}, K_m S_{m2}]$.

Taking into account the dimensional level of K_{ak} and rewriting the linearized representation of the physical model parameters, one has

$$\vartheta = [M_k, J_k, B_{fk}, B_{gk}, B_{sk}, K_{ak}/1e3, A_{fk}, A_{gk}, \bar{d}_{yk}, \bar{d}_{\alpha k}]^T. \qquad (9)$$

Through reasonable analysis, the following assumptions are made for the actual physical system.

Assumption 1: Both the parameter vector and the uncertainty disturbance component in the dual-drive gantry system are bounded and can be expressed as

$$\vartheta \in \Omega_\vartheta \overset{\triangle}{=} \{\vartheta : \vartheta_{\min} \le \vartheta \le \vartheta_{\max}\} \qquad (10)$$

$$\check{d}_p \in \Omega_d \overset{\triangle}{=} \{\check{d}_p : \|\check{d}_p\| \le \varrho_p\} \qquad (11)$$

where $\vartheta_{\min}$ and $\vartheta_{\max}$ are known constant vectors, and ϱ_p is a known design function.

Before designing the synchronous controller, it is necessary to clarify that the expected input of the system is $p_d = [y_d(t), 0]^T$, and the resulting error vector $e = [y_G(t) - y_d(t), \alpha(t)]^T$.

III. SYNCHRONOUS CONTROLLER DESIGN

The proposed composite adaptive synchronous control for the dual-drive gantry stage with load movement, depicted in Fig. 2, is used to deal with various uncertainties and nonlinear

disturbances (e.g., friction, unmodeled dynamics, measurement noise, load changes, and environmental disturbances) in the system. It consists of a parameter estimation module (green box), an expected model compensation module (orange box), and fast model compensation and robust feedback module (blue boxes). In addition, the asymptotic convergence of parameter estimation is guaranteed under the condition of continuous excitation. The dynamic centroid position calculation link (yellow box) is used as bridge between the centroid position of the beam and the load motion, which facilitates reasonable thrust distribution and ensures good steady-state and transient system performance. The detailed controller design process is described in the following subsections.

A. ADAPTIVE LAW

Using known parameter priors to construct adaptive laws, and a projection-type adaptive law with rate limitation is introduced as

$$\dot{\hat{\vartheta}} = \text{sat}_{\dot{\hat{\vartheta}}_M}\left(Proj_{\hat{\vartheta}}(\Gamma \tau)\right) \quad \hat{\vartheta}(0) \in \Omega_\vartheta \qquad (12)$$

where $\dot{\hat{\vartheta}}_M$ is the preset upper bound of the adaptation rate, and Γ and τ represent the adaptive rate matrix and the estimation function to be designed, respectively. The mathematical form of the saturation function $\text{sat}_{\dot{\hat{\vartheta}}_M}(\bullet)$ is given by

$$\text{sat}_{\dot{\hat{\vartheta}}_M}(\bullet) = s_0 \bullet, \ s_0 = \begin{cases} 1, & \text{if } \|\bullet\| \le \dot{\hat{\vartheta}}_M \\ \dfrac{\dot{\hat{\vartheta}}_M}{\|\bullet\|}, & \text{if } \|\bullet\| > \dot{\hat{\vartheta}}_M \end{cases}. \qquad (13)$$

Furthermore, the standard projective adaptation rate is expressed as

$$\text{Proj}_{\hat{\vartheta}}(\bullet) = \begin{cases} \left(I - \Gamma \dfrac{n_{\hat{\vartheta}} n_{\hat{\vartheta}}^T}{n_{\hat{\vartheta}}^T \Gamma n_{\hat{\vartheta}}}\right) \bullet, & \hat{\vartheta} \in \partial\Omega_\vartheta \text{ and } \bullet n_{\hat{\vartheta}}^T > 0 \\ \bullet, & \hat{\vartheta} \in \vec{\Omega}_\vartheta \text{ or } \bullet n_{\hat{\vartheta}}^T < 0 \end{cases} \qquad (14)$$

where $n_{\hat{\vartheta}}^T$ denotes the unit normal vector outward at $\hat{\vartheta} \in \partial\Omega_\vartheta$, and $\partial\Omega_\vartheta$ and $\vec{\Omega}_\vartheta$ are the boundary and interior of Ω_ϑ, respectively.

Lemma 1 (see[23]): Using the rate-limiting projection type adaptive law to update parameters, the following properties apply for any τ:

P1. $\vartheta_{i\,\min} \le \hat{\vartheta}_i(t) \le \vartheta_{i\,\min}, i = 1, 2, \ldots, 9, 10$;

P2. $\tilde{\vartheta}^T\left(\Gamma^{-1}\text{Proj}_{\hat{\vartheta}}(\Gamma \tau) - \tau\right) \le 0, \forall\tau$;

P3. $\|\dot{\hat{\vartheta}}(t)\| \le \dot{\hat{\vartheta}}_M, \forall t$.

B. PROPOSED COMPOSITE ADAPTIVE CONTROL

Model compensation and robust feedback are modularly designed to reduce error tracking. Sliding-mode variables are introduced to simplify the design process

$$\varepsilon = \dot{e} + \zeta e \qquad (15)$$

where ζ is a 2×2 positive definite diagonal matrix. Therefore, the first-order inertia transfer function form of (15) makes ε and e have the same convergence property, i.e., $\varepsilon \to 0$ with

$e \to 0$. Next, a semi-positive definite energy function is defined as

$$V(t) = \frac{1}{2}\varepsilon^T M_p \varepsilon + \frac{1}{2}e^T K_e e \tag{16}$$

where K_e is a positive diagonal matrix to be designed. Differentiating $V(t)$ and substituting (8), the result after simplification yields

$$\dot{V}(t) = \varepsilon^T \left[\upsilon + \left(\bar{d}_p - M_p \ddot{p}_d - B_p \dot{p}_d - K_p p_d - A_p S_f(\dot{p}_d) \right. \right.$$
$$\left. - B_p \dot{e} - K_p e - A_p g_f \dot{e} + M_p \zeta \dot{e} \right) + \check{d}_p \Big] + e^T K_e \dot{e}$$
$$= \varepsilon^T \left[\upsilon + \Phi(p, \dot{p}, t)\vartheta + \check{d}_p \right] + e^T K_e \dot{e} \tag{17}$$

where $g_f \dot{e} = S_f(\dot{p}) - S_f(\dot{p}_d)$ represents the expected approximation error component in Coulomb friction. $\Phi(p, \dot{p}, t)$ is called a regressor matrix with parameters, which can be decomposed into two parts: expected regressor matrix and regressor residual matrix

$$\Phi(p, \dot{p}, t) = \Phi_d(p_d, \dot{p}_d, \ddot{p}_d, t) + \tilde{\Phi}(e, \dot{e}, t) \tag{18}$$

and, one has

$$\Phi_d(p_d, \dot{p}_d, \ddot{p}_d, t)\vartheta = \bar{d}_p - M_p \ddot{p}_d - B_p \dot{p}_d$$
$$- K_p p_d - A_p S_f(\dot{p}_d). \tag{19}$$

From [30], $\tilde{\Phi}(e, \dot{e}, t)$ satisfies

$$\|\tilde{\Phi}\vartheta\| \leq \ell_1 \|e\| + \ell_2 \|e\|^2 + \ell_3 \|\varepsilon\| + \ell_4 \|\varepsilon\|\|e\| \tag{20}$$

where ℓ_i, $(i = 1, 2, 3, 4)$ is the corresponding constant coefficient.

As analyzed in (17)–(19), the expectation compensation technique is used to replace the regressor Φ_d with only expectation information for Φ for parameter learning and estimation, which avoids measurement noise pollution. The control law of the closed-loop system is designed as

$$\upsilon = \begin{cases} \upsilon = \upsilon_a + \upsilon_s \\ \upsilon_a = \upsilon_{a1} + \upsilon_{a2} \\ \upsilon_s = \upsilon_{s1} + \upsilon_{s2} \\ \upsilon_{a1} = -\Phi_d \hat{\vartheta} \\ \upsilon_{s1} = -K_{s1}\varepsilon - K_e e - K_a \|e\|^2 \varepsilon \end{cases} \tag{21}$$

where υ_a and υ_s are the control inputs of the system. υ_{a1} is the expected model compensation term, and the parameter estimation value $\hat{\vartheta}$ can be guaranteed by adaptive rate (12); υ_{a2} is the fast dynamic model compensation term, introduced below; υ_s is an integrated robust feedback term, used to ensure system robustness, which can be divided into two parts, υ_{s1} and υ_{s2} according to different uses; K_{s1}, K_e, and K_a are positive definite diagonal matrices designed to satisfy

$$\sigma_{\min}(K_{s1}) \geq \frac{1}{2}\ell_1 + \ell_3 + \frac{1}{4}\ell_4$$

$$\sigma_{\min}(K_e\zeta) \geq \frac{1}{2}\ell_1 + \frac{1}{4}\ell_2$$

$$\sigma_{\min}(K_a) \geq \ell_2 + \ell_4 \tag{22}$$

that guarantees that $Q > 0$, i.e.,

$$Q = \begin{bmatrix} \sigma_{\min}(K_e\zeta) - \frac{1}{4}\ell_2 & -\frac{1}{2}\ell_1 \\ -\frac{1}{2}\ell_1 & \sigma_{\min}(K_{s1}) - \ell_3 - \frac{1}{4}\ell_4 \end{bmatrix}. \tag{23}$$

Noting (17) and (21), the residual model residuals are defined as

$$-\Phi_d\tilde{\vartheta} + \tilde{d}_p = d_{p*} + d_p^* \tag{24}$$

where the low-frequency component d_{p*} can be processed by the compensation term of the fast dynamic model, whose specific form is

$$\upsilon_{a2} = -\hat{d}_{p*}, \quad \dot{\hat{d}}_{p*} = \text{Proj}_{\hat{d}_{p*}}(\varphi\varepsilon) \text{ and } |\hat{d}_{p*}| \leq d_{p*\max} \tag{25}$$

where φ and $d_{p*\max}$ denote the adaptive gain matrix and the upper bound of model compensation, respectively. An example of nonlinear robustness υ_{s2} is given by

$$\upsilon_{s2} = -K_{s2}\varepsilon, \quad K_{s2} \geq \left(\iota_1 + \iota_2 \|\Phi_d\|^2 + \iota_3 \right) \tag{26}$$

that satisfies

$$\varepsilon^T \left\{ \upsilon_{s2} - \tilde{d}_{p*} + d_p^* \right\} \leq \hbar$$
$$\varepsilon^T \upsilon_{s2} \leq 0 \tag{27}$$

where $\hbar = \hbar_1 \varrho_p^2 + \hbar_2 \|\tilde{\vartheta}\|^2 + \hbar_3 d_{p*\max}^2$ is used to quantify the remaining model residuals and uncertainties. In addition, both $\hbar_i$ and ι_i are positive constants with $\iota_i = \frac{1}{4\hbar_i}$, $i = 1, 2, 3$.

Theorem 1: The control law (21) and adaptation rate (12), (25) are applied to the dual-drive gantry system, which enables all signals to be bounded. For $V(t)$, one has

$$V(t) \leq \exp(-\eta t)V(0) + \frac{\hbar}{\eta}\left[1 - \exp(-\eta t) \right] \tag{28}$$

where $\eta = 2\sigma_{\min}(Q)/\{\max[\sigma_{\max}(M_p), \sigma_{\max}(K_e)]\}$.

Proof: Simplification by introducing (15), (18), (21), (24), and (25) into (17) yields

$$\dot{V}(t) = \varepsilon^T \left[-\Phi_d \hat{\vartheta} + \upsilon_{a2} + \upsilon_s + \Phi_d \vartheta + \tilde{\Phi}\vartheta + \check{d}_p \right] + e^T K_e \dot{e}$$
$$= \varepsilon^T \left[-\hat{d}_{p*} + \upsilon_s - \Phi_d \tilde{\vartheta} + \check{d}_p + \tilde{\Phi}\vartheta \right] + e^T K_e \dot{e}$$
$$= \varepsilon^T \left[\upsilon_s - \tilde{d}_{p*} + d_p^* + \tilde{\Phi}\vartheta \right] + e^T K_e \dot{e}$$
$$\leq \varepsilon^T \left[\upsilon_{s1} + \upsilon_{s2} - \tilde{d}_{p*} + d_p^* \right] + \|\varepsilon\|\|\tilde{\Phi}\vartheta\| + e^T K_e \dot{e}. \tag{29}$$

Further introducing (20), (22), (23), and (27), one has

$$\dot{V}(t) \leq \varepsilon^T \left(\upsilon_{s2} - \tilde{d}_{p*} + d_p^* \right) - K_{s1}\|\varepsilon\|^2 - K_a\|e\|^2\|\varepsilon\|^2$$
$$+ \ell_1 \|\varepsilon\|\|e\| + \ell_2 \|\varepsilon\|\|e\|^2 + \ell_3 \|\varepsilon\|^2 + \ell_4 \|\varepsilon\|^2\|e\|$$
$$- K_e \zeta \|e\|^2$$
$$\leq -\sigma_{\min}(\ell_2 + \ell_4)\|e\|^2\|\varepsilon\|^2 - \sigma_{\min}(K_{s1})\|\varepsilon\|^2$$
$$- \sigma_{\min}(K_e\zeta)\|e\|^2 + \ell_1\|\varepsilon\|\|e\| + \ell_2\|\varepsilon\|\|e\|^2 + \ell_3\|\varepsilon\|^2$$
$$+ \ell_4\|\varepsilon\|^2\|e\| + \hbar$$

$$
\begin{aligned}
&\leq -\ell_2 \left[\|\varepsilon\| - \frac{1}{2} \right]^2 \|e\|^2 - \ell_4 \left[\|e\| - \frac{1}{2} \right]^2 \|\varepsilon\|^2 \\
&\quad - \left[\sigma_{\min}(K_{s1}) - \ell_3 - \frac{1}{4}\ell_4 \right] \|\varepsilon\|^2 + \ell_1 \|\varepsilon\| \|e\| \\
&\quad - \left[\sigma_{\min}(K_e \zeta) - \frac{1}{4}\ell_2 \right] \|e\|^2 + \hbar \\
&\leq -z^T Q z + \hbar \\
&\leq -\eta V + \hbar
\end{aligned} \tag{30}
$$

where $z = [\|e\|, \|\varepsilon\|]^T$, and Theorem 1 is proved.

C. PARAMETER ESTIMATION ALGORITHM

The closed-loop system guarantees the boundedness of all signals under control law (21) and adaptive rate (12), which allows various reasonable estimation methods to be applied to identify unknown parameters. Consequently, it is necessary to design an estimation algorithm with good enough convergence characteristics to achieve asymptotic convergence of the final output tracking and parameter estimation of the system. Assuming that there is only parameter uncertainty in the system (i.e., $\check{d}_p = 0$), (8) can be rewritten as

$$
\upsilon_f = \psi_f^T \vartheta \tag{31}
$$

where ψ_f^T is the regressor matrix processed by the fourth-order Butterworth filter H_f. The resulting estimation error is

$$
\epsilon_p = \psi_f^T \left(\hat{\vartheta} - \vartheta \right) = \psi_f^T \tilde{\vartheta}. \tag{32}
$$

The standard recursive least squares estimator (RLSE) with forgetting property is very effective for parameter estimation of slow time-varying systems. Considering that the constant forgetting factor may induce unbounded gain (i.e., $\sigma_{\max}(\Gamma(t)) \to \infty$) when the continuous excitation of the system is not satisfied, it is necessary to add constraints to the RLSE algorithm. Hence, a bounded-gain-forget estimation algorithm with exponential convergence is introduced

$$
\dot{\Gamma} = \begin{cases} \mu\Gamma - \dfrac{\Gamma \psi_f \psi_f^T \Gamma}{1 + \upsilon tr\left\{ \psi_f^T \Gamma \psi_f \right\}}, & \text{if } \sigma_{\max}(\Gamma(t)) \leq \rho_m \\ 0, & \text{else} \end{cases} \tag{33}
$$

$$
\tau = -\frac{\psi_f \epsilon_p}{1 + \upsilon tr\{\psi_f^T \Gamma \psi_f\}} \tag{34}
$$

where μ is a forgetting factor and ρ_m represents the preset upper bound of $\Gamma(t)$, respectively. υ is the normalization coefficient and $tr(\bullet)$ is the trace operation.

Lemma 2 (see [23]): Selecting rate-limited projection adaptation rate (16) and estimator (33), (34), the following properties result:

P4. $\Gamma(t) \leq \rho_m I$;
P5. $\tilde{\vartheta} \in \mathcal{L}_\infty[0, \infty)$;
P6. $\hat{\vartheta}, \epsilon_p \in \mathcal{L}_2[0, \infty) \cap \mathcal{L}_\infty[0, \infty)$.

Theorem 2: If $\check{d}_p = 0$ with $\forall t \geq t_0$ and matrix ψ_f satisfies persistent excitation, i.e., there exists a constant λ for any

$T > 0$, such as

$$
\int_t^{t+T} \psi_f^T \psi_f \geq \lambda I \tag{35}
$$

in addition to deducing Theorem 1, the control law (21) can ensure asymptotic convergence of parameter estimation and achieve zero-error tracking of the system.

Proof: Noting (32), (35), and (P6), one has

$$
\tilde{\vartheta}^T \int_t^{t+T} \psi_f^T(\upsilon)\psi_f(\upsilon)d\upsilon\tilde{\vartheta} = \int_t^{t+T} \epsilon_p^T(\upsilon)\epsilon_p(\upsilon)d\upsilon
$$
$$
\geq \lambda\|\tilde{\vartheta}\|^2 \to 0 \text{ as } t \to \infty. \tag{36}
$$

Obviously, $\tilde{\vartheta}$ converges asymptotically to 0, i.e., $\tilde{\vartheta} \to 0$ when $t \to \infty$. Additionally, a new energy function is redefined as

$$
\dot{V}' = V + \frac{1}{2}\hat{d}_{p*}^T \varphi^{-1}\hat{d}_{p*}. \tag{37}
$$

Differentiating $\dot{V}'$ and substituting (30), the simplified result is

$$
\begin{aligned}
\dot{V}' &\leq -z^T Q z + \varepsilon^T \left(\upsilon_{s2} - \tilde{d}_{p*} + d_p^* \right) + \hat{d}_{p*}^T \varphi^{-1}\dot{\hat{d}}_{p*} \\
&\leq -z^T Q z + \varepsilon^T \left(-\hat{d}_{p*} + d_{p*} + d_p^* \right) + \hat{d}_{p*}^T \varphi^{-1}\dot{\hat{d}}_{p*} \\
&= -z^T Q z + \varepsilon^T \left(-\hat{d}_{p*} - \Phi_d \tilde{\vartheta} \right) + \hat{d}_{p*}^T \varphi^{-1}\dot{\hat{d}}_{p*} \\
&= -z^T Q z - \varepsilon^T \Phi_d \tilde{\vartheta} + \hat{d}_{p*}^T \left(\varphi^{-1}\dot{\hat{d}}_{p*} - \varepsilon \right) \\
&\leq -z^T Q z - \varepsilon^T \Phi_d \tilde{\vartheta}
\end{aligned} \tag{38}
$$

Φ_d is bounded from Theorem 1 and $\tilde{\vartheta} \in \mathcal{L}_2$, which guarantees that $\Phi_d \tilde{\vartheta} \in \mathcal{L}_2$. Consequently, $\varepsilon \in \mathcal{L}_2$ and $z \in \mathcal{L}_2$ can be easily obtained from (38). Using Babarlat's theorem, asymptotic tracking of the system is proved, i.e., $e \to 0$ when $t \to \infty$.

Remark 1: The principle of composite adaptive control is to combine the adaptive law based on error tracking ε and the parameter estimation law based on prediction error ϵ_p and design (25) and (34) separately. Fast convergence of control system parameters and small tracking error can be achieved even in the presence of parameter uncertainties.

IV. IDENTIFICATION EXPERIMENT

This section describes the frequency domain identification experiment carried out to verify the high-frequency flexible modes existing in the dynamic model of the dual-drive gantry system. The relationship between center of mass position and load position change can be obtained from the dynamic response in the frequency domain. A gantry stage from Arkbis Company has been used in the experiment. The nominal mass values of the mechanical beam and the moving head are 25 Kg and 11 Kg, respectively. The maximum thrust generated by the Y-axis linear motor is 2830 N, the maximum peak current it can withstand is 18 Arms, and the force constant is $K_F = 157.2$ N/Arms.
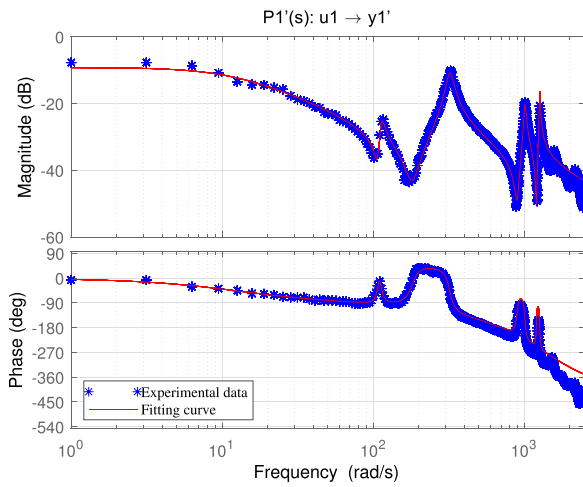
FIGURE 3. Frequency domain response and identification results of U_1 to $\dot{y}_1$.
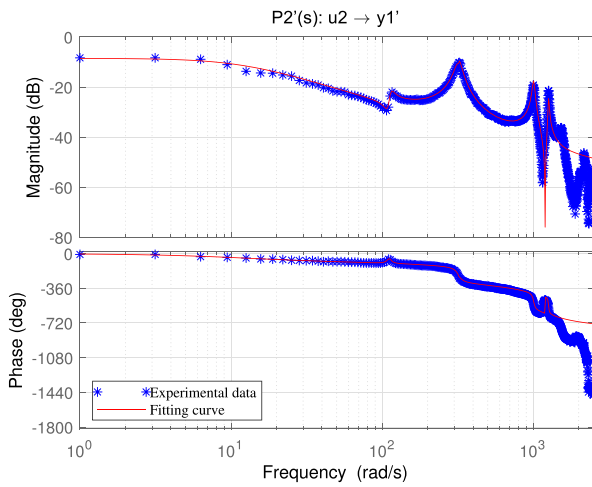

FIGURE 4. Frequency domain response and identification results of U_2 to $\dot{y}_1$.

Considering that the excitation signal should contain as many different frequency components as possible, to avoid repeating experiments a superposition sinusoidal signal is used as input. The sequence generated by *[sinesum,frequs]=idinput([10000,1,5], 'sine,' [0,1], [-1,1], [4999,50,1])* in MATLAB is used to drive the two Y axes. When the moving head is in the center position, the output frequency domain response results ($U_i \rightarrow \dot{y}_1$) are processed using the system identification and curve fitting methods, as shown in Figs. 3 and 4. Identification results can be expressed in the form of the following piecewise transfer function cascade:

$$P'(s) = G_1(s) \cdot G_2(s) \cdot G_3(s) \cdot G_4(s) \tag{39}$$

where $G_1(s)$ and $G_3(s)$ correspond to the fully rigid model and the mainly flexible damping model in (7), respectively. $G_2(s)$ is the flexible component at low frequencies and $G_4(s)$ represents the unmodeled dynamics and uncertainties of the system at higher frequencies.

The corresponding transfer functions identified from Figs. 3 and 4 are, respectively

$$G_1(s) = \frac{1}{0.24s + 2.978}$$

$$G_2(s) = \frac{1.12\left(s^2 + 7.004s + 1.137e4\right)}{s^2 + 8.07s + 1.273e4}$$

$$G_3(s) = \frac{3.156\left(s^2 + 30.68s + 3.26e4\right)}{s^2 + 35.33s + 1.029e5}$$

$$G_4(s) = \frac{1.045\left(s^2 + 43.85s + 7.98e5\right)\left(s^2 - 2255s + 2.18e6\right)}{\left(s^2 + 34.19s + 1.015e6\right)\left(s^s + 1930s + 1.572e6\right)}$$

$$\times \frac{s^2 + 16.55s + 1.439e6}{s^2 + 17.26s + 1.595e6} \tag{40}$$

$$G_1(s) = \frac{1.02}{0.24s + 2.978}$$

$$G_2(s) = \frac{1.074\left(s^2 + 8.827s + 1.199e4\right)}{s^2 + 9.208s + 1.288e4}$$

$$G_3(s) = \frac{-1.044\left(s^2 + 1.4s - 9.847e4\right)}{s^2 + 35.13s + 1.028e5}$$

$$G_4(s) = \frac{-2.39\left(s^2 - 7.312s + 1.032e5\right)\left(s^2 - 786.2s + 1.505e6\right)}{\left(s^2 - 7.903s + 1.036e5\right)\left(s^s + 36.9s + 1.014e6\right)}$$

$$\times \frac{\left(s^2 + 1.542s + 1.439e6\right)\left(s - 729.6\right)}{\left(s^2 + 21.84s + 1.599e6\right)\left(s + 2125\right)}. \tag{41}$$

As expected, experimental results show the existence of high-frequency flexible features. It can be seen from the figure that high-frequency flexible dynamics are excited when frequency exceeds 100 rad/s. The identified inertia mass parameter $\hat{M}_k = 0.24$, which is similar to the result obtained by time-domain least squares identification (mentioned below), also indicates the validity of the experimental results. In addition, the identification results show that the resonant and antiresonant frequencies of the system are $\omega_r = 320.78$ rad/s and $\omega_{ar} = 180.55$ rad/s, respectively, which can be verified by comparison of experimental curves.

In order to obtain the relationship between the centroid of the beam and the X-axis displacement, the centroid offset in the generalized coordinate system is defined as

$$x_g(x) = \frac{M_x(x + x_0)}{My} \tag{42}$$

where M_x is the mass of the moving head and load, x and x_0 are the position information feedback from the grating encoder and the initial deviation between the centroid of the working head and the measurement, respectively.

Introducing the centroid coefficient, one has

$$\beta(x) = \frac{S_{m2}(x)}{S_{m1}(x)} = \frac{\frac{S_m}{2} - x_g(x)}{\frac{S_m}{2} + x_g(x)} = \frac{\eta_1 - x}{\eta_2 + x} \tag{43}$$

TABLE 1. Frequency Domain Identification Results

Index	$x = -0.2m$	$x = 0$	$x = 0.2m$
Ξ_1	2.857	3.156	3.482
Ξ_2	−1.318	−1.044	−0.886
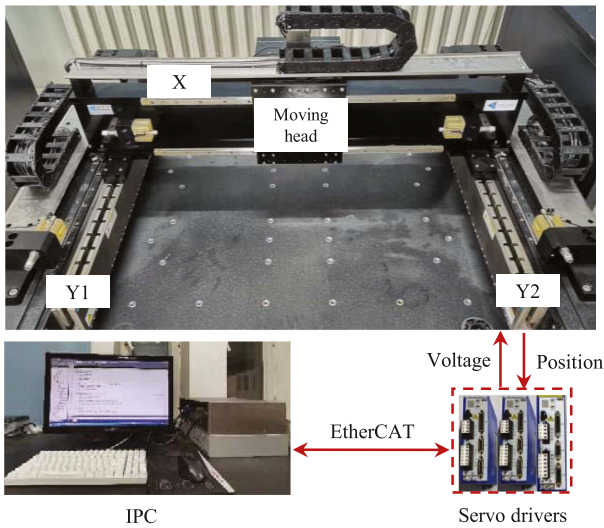
FIGURE 5. Experimental dual-drive gantry system stage.

where $\eta_1 = \frac{M_y}{2M_x} S_m - x_0$ and $\eta_2 = \frac{M_y}{2M_x} S_m + x_0$ are constant values, which can be approximated by the experimental results of several groups of identification when the payload is at different positions.

Noting the transfer function form of the high-frequency components in (7), it yields

$$\beta = \frac{1 - \Xi_2}{\Xi_1 - 1} \qquad (44)$$

where $\Xi_1 = 1 + \frac{M_k S_{e1} S_{m1}}{J_k}$ and $\Xi_2 = 1 - \frac{M_k S_{e1} S_{m2}}{J_k}$.

Three groups of frequency domain identification results of the moving head at different positions are listed on Table 1.

From the identified characteristic data and (43), $\eta_1 = 1.627$ and $\eta_2 = 1.678$ can be easily obtained. Consequently, $\beta(x) = \frac{1.627 - x}{1.678 + x}$, which is used as thrust allocation calculation module in the following section.

V. COMPARATIVE EXPERIMENTS
A. EXPERIMENT SETUP

Comparative experiments have been carried out in the dual-drive gantry system shown in Fig. 5. The industrial programmable computer is used to run different control algorithms. It sends motion commands to the servo drive system through the EntherCAT protocol. The control voltage/current generated by the servo driver is used to drive the axis movement of the gantry stage. The position signal generated by the motion is detected by an optical encoder and then fed back to form a closed-loop motion system. The detection accuracy of the encoder is 50 nm and the span of the beam is $S_e = 1.185$ m, $S_g = 1.095$ m, and $S_m = 0.975$ m.
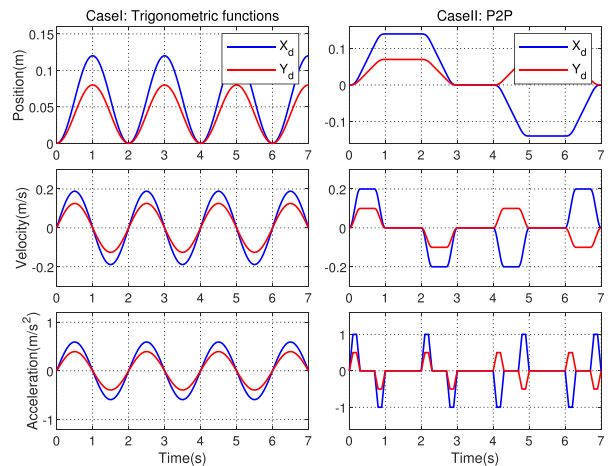
FIGURE 6. Expected trajectories for comparison experiments.

B. PARAMETER SETTING

The least square method is used for off-line parameter identification. Nominal system parameter values are $K_m = 1.02$ and $\hat{\vartheta}(0) = [0.2, 0.02, 0.01, 0.05, 1.9, 1.74, 0.03, 0, 0, 0]$. The upper and lower bounds of parameter estimation are reasonably set as $\vartheta_{\min} = [0.18, 0.01, 0.01, -0.1, 1, 1, 0.01, -0.01, -0.04, -0.01]$ and $\vartheta_{\max} = [0.28, 0.03, 0.22, 0.1, 2.6, 3, 0.05, 0.01, 0.04, 0.01]$.

The thrust distributions achieved by combining (8) and (43) system Y axes are calculated as

$$u_1 = \frac{S_m \beta(x) \upsilon_1 - (1 + \beta(x)) \upsilon_2}{S_m (1 + \beta(x))}$$

$$u_2 = \frac{S_m \upsilon_1 + (1 + \beta(x)) \upsilon_2}{K_m S_m (1 + \beta(x))}. \qquad (45)$$

As shown in Fig. 6, the expected Y-axis trajectories are selected as trigonometric (Case I) and point-to-point (P2P, Case II) motion modes for the experiments to verify the effectiveness of the proposed synchronous control scheme. It should be noted that the input signal xd is only used for the expected trajectory of the load motion in the experiment, and has no special effect.

The following three groups of control algorithms have been tested in the comparative experiments.

C1: The composite adaptive control algorithm proposed in this article. Nonlinear Coulomb friction is simplified as $\frac{2}{\pi} \arctan(500\dot{p})$ and sliding-mode gain matrix is chosen as $\zeta = \text{diag}[70, 50]$. The simplified robust feedback term $\upsilon_s = -K_s \varepsilon - K_e e - K_a \|e\|^s \varepsilon$ (including K_{s1} and K_{s2} in K_s), with control gain matrices $K_s = \text{diag}[7, 2]$, $K_e = \text{diag}[200, 200]$, and $K_a = \text{diag}[300, 300]$. The initial value of the learning rate for parameter estimation is designed to be $\Gamma(0) = \text{diag}[100, 100, 100, 100, 100, 100, 100, 100, 100, 100]$, and its preset upper bound $\rho_m = 5000$. The forgetting factor and standardization coefficient of the correlation coefficient are $\mu = 0.02$ and $\nu = 0.1$, respectively. The adaptive rate of the design error
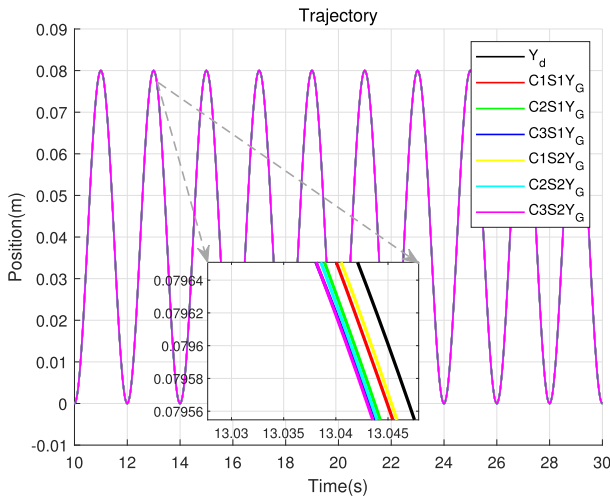
FIGURE 7. Trace of the trigonometric function curve.

FIGURE 8. Tracking error in Case I.

tracking is $\varphi = \text{diag}[60, 15]$, and its upper bound is chosen as $d_{p*\max} = [0.1, 0.1]^T$.

C2: Neural network based ARC (NNARC) algorithm: The neural network part selects the Gaussian function, and its center value and width are designed as $c_{nj} = [-0.21, -0.14, -0.07, 0, 0.07, 0.14, 0.21]_{5\times 7}$ and $b_j = [10, 10, 10, 10, 10, 10, 10]$. The learning rate matrix and robust gain coefficient are selected as $\varpi = \text{diag}[5, 5, 5, 5, 5, 5, 5]$ and $\kappa = 0.05$. The adaptive rate in the ARC part is $\Gamma = \text{diag}[10, 0, 200, 30, 0, 0, 80, 50, 50, 50]$. The other parameters are the same as in C1.

C3: Direct/indirect adaptive robust control (DCARC) algorithm: The corresponding robust parameters and adaptive law gain matrix are consistent with C1 and C2 to ensure the fairness of the experiment.

Set1: Thrust distribution based on the position relationship of the centroid. Combined with the experimental results of frequency domain identification, the centroid coefficient $\beta(x) = \frac{1.627-x}{1.678+x}$ is applied to the final thrust distribution.

Set2: Calculation of thrust distribution regardless of centroid factor. Centroid factor set to constant $\beta(x)=1$ even with load motion.

Evaluation indexes $L[\bullet]_2 = \sqrt{\left(\int_0^T |\bullet|^2 dt\right)/T}$ and $L[\bullet]_\infty = \max(|\bullet|)$ [25] are used to evaluate the performance and effectiveness of the different controllers.

C. ANALYSIS OF THE RESULTS

Case I: Fig. 7 shows the motion trajectory of the beam tracking trigonometric function curve under different settings. The proposed control algorithm C1 achieves better tracking accuracy than NNARC and DCARC. With C2 and C3, better results are obtained for Set1 than for Set2. The tracking error and rotation angle curves of the gantry system during movement are depicted in Figs. 8 and 9, respectively,
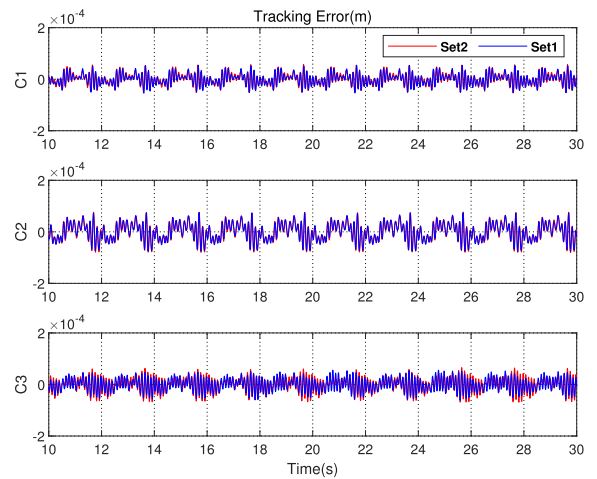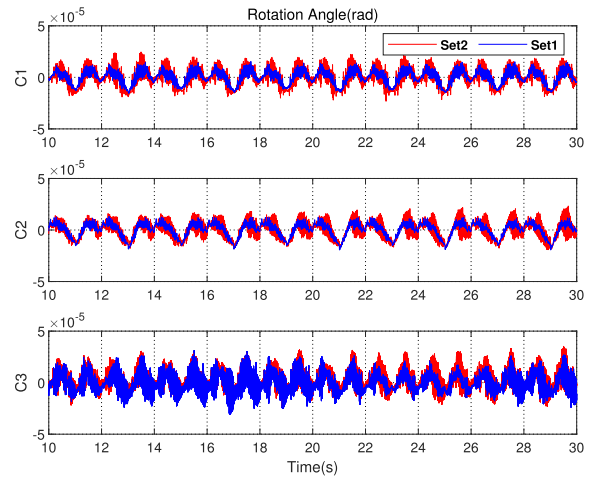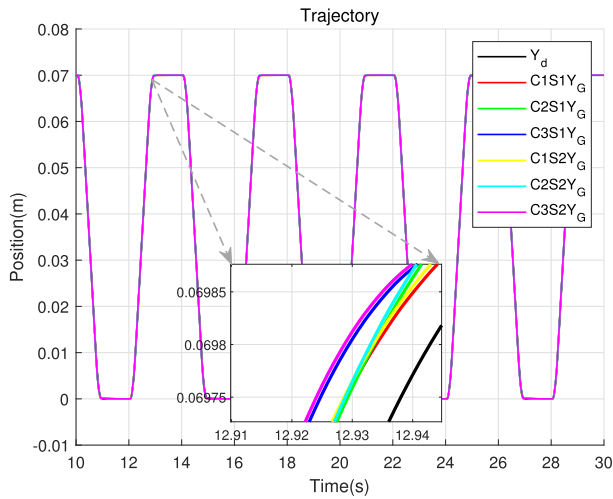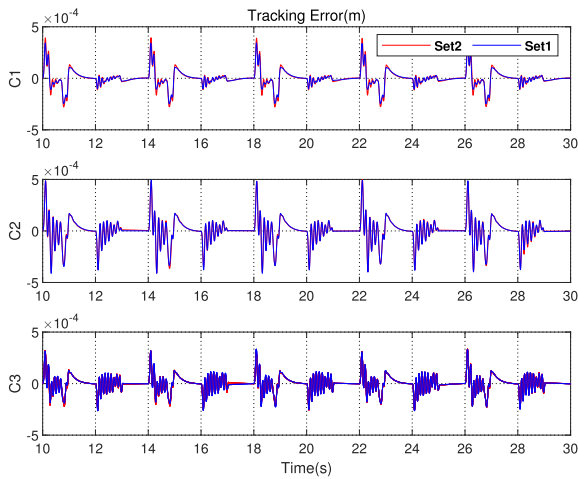

FIGURE 9. Rotation angle in Case I.

TABLE 2. Performance Index in Case I

Index	$L[e]_2$	$L[e]_\infty$	$L[\alpha]_2$	$L[\alpha]_\infty$
units	μm		μrad	
C1(Set1)	20.961	54.520	6.194	15.450
C2(Set1)	32.932	76.524	6.731	19.322
C3(Set1)	24.349	61.377	9.047	31.151
C1(Set2)	21.321	57.735	8.528	24.634
C2(Set2)	33.415	80.297	8.051	23.264
C3(Set2)	26.432	69.293	9.718	35.147

and its performance index results are listed on Table 2. Tracking errors of C1 are the best, only 20.961 μm and 54.520 μm. Tracking accuracy for Set2 is lower than that for Set1. Root mean square and maximum error values of C2 reach 33.415 μm and 80.297 μm. It is noted that load motion has a large impact on the accuracy of the two-axis synchronization, and that the blue curve fluctuates smoothly in different experiments. Therefore, for the synchronous control of high-precision equipment, the influence caused by the

FIGURE 10. Trace of the P2P curve.

FIGURE 11. Tracking error in Case II.

FIGURE 12. Rotation angle in Case II.

TABLE 3. Performance Index in Case II

Index	$L[e]_2$	$L[e]_\infty$	$L[\alpha]_2$	$L[\alpha]_\infty$
units	μm		μrad	
C1(Set1)	75.173	342.96	14.092	34.042
C2(Set1)	114.79	493.70	14.822	31.687
C3(Set1)	75.382	333.29	18.924	42.663
C1(Set2)	84.480	394.40	16.041	44.378
C2(Set2)	113.95	502.35	14.969	44.926
C3(Set2)	74.509	334.85	20.048	44.839

FIGURE 13. Parameter estimation convergence.

load movement cannot be simply regarded as interference and ignored. Results on Table 2 again verify the importance and usefulness of the relationship between beam centroid and load motion presented in this article.

Case II: The real-time trajectory results of the beam tracking the P2P expected curve are presented in Fig. 10. Tracking performance analyses are the same as for Case I. Figs. 11 and 12 show the different error curves obtained. Tracking and synchronization performance are consistent with expectations. Combined with the experimental data on Table 3, the proposed control method achieves both good tracking and synchronization control accuracy, and its performance is improved by 34.5% and 29.7%, respectively, compared with the unbearable experimental results. C2 achieves a good synchronization control accuracy despite ignoring the influence of load motion, and the synchronization performance index of C1 increases from 14.092 μm to 16.041 μm under the same setting. The root cause is that the neural network compensator has a certain inhibitory effect on the influence of
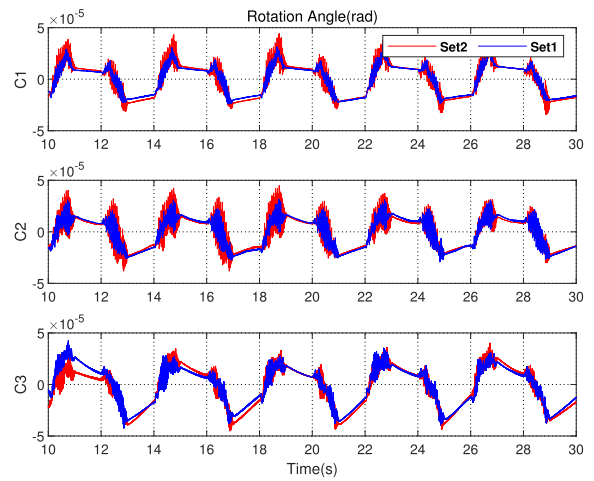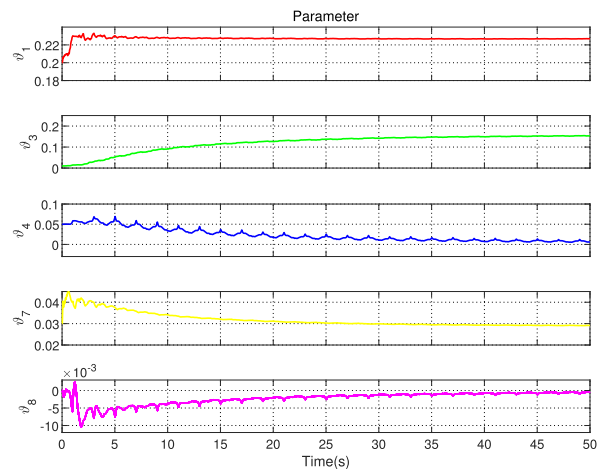
the load movement, but its poor tracking accuracy makes the control scheme have great limitations in practical applications. Comprehensive performance index data analysis shows that the synchronous control scheme proposed in this article has excellent control and performance characteristics.

Fig. 13 shows the change process of the main kinetic parameters. It can be seen that at time = 50 s parameter values have been stabilized. The estimated value of ϑ_1 reaches around 0.24, which is consistent with the previous frequency domain identification results. The same applies to the other

four parameters. The parameters quickly converge to near the true value, which verifies the effectiveness of the designed parameter estimation algorithm.

VI. CONCLUSION

In this article, a synchronous controller is proposed for dual-drive gantry stages with load movement to improve their tracking and synchronization accuracy. Based on the characteristic analysis of mechanically flexible components, a rigid-flexible coupling dynamic model is obtained, which facilitates active control in the rotational dimension to adjust the internal force between shafts. A composite adaptive control algorithm is designed to separate the parameter estimator from the robust control law, which ensures the stability of the system in the presence of parameter uncertainties and unknown disturbances. Furthermore, model parameters are obtained by frequency domain identification to construct the bridge between load motion and the centroid of the beam. The precise control input calculation is distributed to both Y axes to ensure good tracking and synchronization performance of the system. Compared with the existing literature nonlinear control methods (such as NNARC, DCARC, ARC, direct robust control (DRC), and PID), the experimental results show the effectiveness and advantages of the proposed synchronous control strategy.

REFERENCES

[1] K. Tan, S. Lim, S. Huang, H. Dou, and T. Giam, "Coordinated motion control of moving gantry stages for precision applications based on an observer-augmented composite controller," *IEEE Trans. Control Syst. Technol.*, vol. 12, no. 6, pp. 984–991, Nov. 2004.

[2] Y. Liu, W. Sun, C. Buccella, and C. Cecati, "Robust control of dual-linear-motor-driven gantry stage for coordinated contouring tasks based on feed velocity," *IEEE Trans. Ind. Electron.*, to be published, doi: 10.1109/TIE.2022.3199920.

[3] W. Wang, J. Ma, Z. Cheng, X. Li, C. W. de Silva, and T. H. Lee, "Global iterative sliding mode control of an industrial biaxial gantry system for contouring motion tasks," *IEEE/ASME Trans. Mechatron.*, vol. 27, no. 3, pp. 1617–1628, Jun. 2022.

[4] N. Kamaldin, S.-L. Chen, C. S. Teo, W. Lin, and K. K. Tan, "A novel adaptive jerk control with application to large workspace tracking on a flexure-linked dual-drive gantry," *IEEE Trans. Ind. Electron.*, vol. 66, no. 7, pp. 5353–5363, Jul. 2019.

[5] H. Gao, Z. Li, X. Yu, and J. Qiu, "Hierarchical multiobjective heuristic for PCB assembly optimization in a beam-head surface mounter," *IEEE Trans. Cybern.*, vol. 52, no. 7, pp. 6911–6924, Jul. 2022.

[6] Z. Li, X. Yu, J. Qiu, and H. Gao, "Cell division genetic algorithm for component allocation optimization in multifunctional placers," *IEEE Trans. Ind. Informat.*, vol. 18, no. 1, pp. 559–570, Jan. 2022.

[7] C. Hu, T. Ou, H. Chang, Y. Zhu, and L. Zhu, "Deep GRU neural network prediction and feedforward compensation for precision multiaxis motion control systems," *IEEE/ASME Trans. Mechatron.*, vol. 25, no. 3, pp. 1377–1388, Jun. 2020.

[8] B. Yao, C. Hu, L. Lu, and Q. Wang, "Adaptive robust precision motion control of a high-speed industrial gantry with cogging force compensations," *IEEE Trans. Control Syst. Technol.*, vol. 19, no. 5, pp. 1149–1159, Sep. 2011.

[9] Z. Chen, B. Yao, and Q. Wang, "Accurate motion control of linear motors with adaptive robust compensation of nonlinear electromagnetic field effect," *IEEE/ASME Trans. Mechatron.*, vol. 18, no. 3, pp. 1122–1129, Jun. 2013.

[10] L. Lu, B. Yao, Q. Wang, and Z. Chen, "Adaptive robust control of linear motors with dynamic friction compensation using modified LuGre model," *Automatica*, vol. 45, no. 12, pp. 2890–2896, Oct. 2009.

[11] C. Canudas de Wit, H. Olsson, K. Astrom, and P. Lischinsky, "A new model for control of systems with friction," *IEEE Trans. Autom. Control*, vol. 40, no. 3, pp. 419–425, Mar. 1995.

[12] P. Shi, W. Sun, X. Yang, I. J. Rudas, and H. Gao, "Master-slave synchronous control of dual-drive gantry stage with cogging force compensation," *IEEE Trans. Syst. Man Cybern.: Syst.*, vol. 53, no. 1, pp. 216–225, Jan. 2022.

[13] J. Wang, H. Pan, and W. Sun, "Event-triggered adaptive fault-tolerant control for unknown nonlinear systems with applications to linear motor," *IEEE/ASME Trans. Mechatron.*, vol. 27, no. 2, pp. 940–949, Apr. 2022.

[14] W. Sun, Y. Liu, and H. Gao, "Constrained sampled-data ARC for a class of cascaded nonlinear systems with applications to motor-servo systems," *IEEE Trans. Ind. Informat.*, vol. 15, no. 2, pp. 766–776, Feb. 2019.

[15] S.-Y. Chen, H.-H. Chiang, T.-S. Liu, and C.-H. Chang, "Precision motion control of permanent magnet linear synchronous motors using adaptive fuzzy fractional-order sliding-mode control," *IEEE/ASME Trans. Mechatron.*, vol. 24, no. 2, pp. 741–752, Apr. 2019.

[16] C. S. Chen, S. K. Chen, and L. Y. Chen, "Disturbance observer-based modeling and parameter identification for synchronous dual-drive ball screw gantry stage," *IEEE/ASME Trans. Mechatron.*, vol. 24, no. 6, pp. 2839–2849, Dec. 2019.

[17] S. Vazquez et al., "An artificial intelligence approach for real-time tuning of weighting factors in FCS-MPC for power converters," *IEEE Trans. Ind. Electron.*, vol. 69, no. 12, pp. 11987–11998, Dec. 2022.

[18] J. Ma et al., "Robust decentralized controller synthesis in flexure-linked h-gantry by iterative linear programming," *IEEE Trans. Ind. Informat.*, vol. 15, no. 3, pp. 1698–1708, Mar. 2019.

[19] H. Dong, X. Yang, and M. V. Basin, "Practical tracking of permanent magnet linear motor via logarithmic sliding mode control," *IEEE/ASME Trans. Mechatron.*, vol. 27, no. 5, pp. 4112–4121, Oct. 2022.

[20] Y. Liu, W. Sun, and H. Gao, "High precision robust control for periodic tasks of linear motor via b-spline wavelet neural network observer," *IEEE Trans. Ind. Electron.*, vol. 69, no. 8, pp. 8255–8263, Aug. 2022.

[21] K. L. Barton and A. G. Alleyne, "A cross-coupled iterative learning control design for precision motion control," *IEEE Trans. Control Syst. Technol.*, vol. 16, no. 6, pp. 1218–1231, Nov. 2008.

[22] B. Yao and M. Tomizuka, "Adaptive robust control of MIMO nonlinear systems in semi-strict feedback forms," *Automatica*, vol. 37, no. 9, pp. 1305–1321, 2001.

[23] B. Yao and A. Palmer, "Indirect adaptive robust control of SISO nonlinear systems in semi-strict feedback forms," *IFAC Proc. Vol.*, vol. 35, no. 1, pp. 397–402, 2002.

[24] F.-J. Lin, P.-H. Chou, C.-S. Chen, and Y.-S. Lin, "DSP-based cross-coupled synchronous control for dual linear motors via intelligent complementary sliding mode control," *IEEE Trans. Ind. Electron.*, vol. 59, no. 2, pp. 1061–1073, Feb. 2012.

[25] Z. Liu, W. Lin, X. Yu, J. J. Rodríguez-Andina, and H. Gao, "Approximation-free robust synchronization control for dual-linear-motors-driven systems with uncertainties and disturbances," *IEEE Trans. Ind. Electron.*, vol. 69, no. 10, pp. 10500–10509, Oct. 2022.

[26] P. Shi, W. Sun, and X. Yang, "RBF neural network-based adaptive robust synchronization control of dual drive gantry stage with rotational coupling dynamics," *IEEE Trans. Autom. Sci. Eng.*, to be published on, doi: 10.1109/TASE.2022.3177540.

[27] D. Sun, X. Shao, and G. Feng, "A model-free cross-coupled control for position synchronization of multi-axis motions: Theory and experiments," *IEEE Trans. Control Syst. Technol.*, vol. 15, no. 2, pp. 306–314, Mar. 2007.

[28] Z. Chen, B. Yao, and Q. Wang, "μ-synthesis-based adaptive robust control of linear motor driven stages with high-frequency dynamics: A case study," *IEEE/ASME Trans. Mechatron.*, vol. 20, no. 3, pp. 1482–1490, Jun. 2015.

[29] C. Li, B. Yao, and Q. Wang, "Modeling and synchronization control of a dual drive industrial gantry stage," *IEEE/ASME Trans. Mechatron.*, vol. 23, no. 6, pp. 2940–2951, Dec. 2018.

[30] C. Li, Z. Chen, and B. Yao, "Adaptive robust synchronization control of a dual-linear-motor-driven gantry with rotational dynamics and accurate online parameter estimation," *IEEE Trans. Ind. Informat.*, vol. 14, no. 7, pp. 3013–3022, Jul. 2018.

[31] C. Li, C. Li, Z. Chen, and B. Yao, "Adaptive thrust allocation based synchronization control of a dual drive gantry stage," *Mechatron.*, vol. 54, pp. 68–77, 2018.

PENGWEI SHI received the B.S. degree in automation from the Shandong University of Science and Technology, Qingdao, China, in 2018. He is currently working toward the Ph.D. degree in control science and engineering from the Harbin Institute of Technology, Harbin, China.

His research interests include adaptive control and mechatronic systems.

XINGHU YU was born in Yantai, China, in 1988. He received the M.M. degree in osteopathic medicine from Jinzhou Medical University, Jinzhou, China, in 2016 and the Ph.D. degree in control science and engineering from the Harbin Institute of Technology, Harbin, China, in 2020.

He is currently the Chief Executive Officer with the Ningbo Institute of Intelligent Equipment Technology Company, Ltd., Ningbo, China. He has authored more than ten technical papers of conference proceedings and refereed journals, including the IEEE TRANSACTIONS JOURNALS, and holds 20 invention patents. His research interests include switched systems, intelligent control, and biomedical image processing.

XUEBO YANG (Member, IEEE) received the B.S. degree in automation from Northeast Forestry University, Harbin, China, in 2004, the M.S. degree in control science and engineering from Harbin Engineering University, Harbin, in 2007, and the Ph.D. degree in control science and engineering from the Harbin Institute of Technology, Harbin, in 2011.

He is currently a Professor with the Research Institute of Intelligent Control Systems, Harbin Institute of Technology. His current research interests include robust and adaptive control theory and applications, spacecraft orbital, and attitude control.

JUAN J. RODRÍGUEZ-ANDINA (Fellow, IEEE) received the M.Sc. degree in electrical engineering from the Technical University of Madrid, Madrid, Spain, in 1990 and the Ph.D. degree in electrical engineering from the University of Vigo, Vigo, Spain, in 1996.

He is currently a Professor with the Department of Electronic Technology, University of Vigo. From 2010 to 2011, he was on Sabbatical Leave as a Visiting Professor with the Advanced Diagnosis, Automation, and Control Laboratory, North Carolina State University, Raleigh, NC, USA. From 2015 to 2017, he was with the Harbin Institute of Technology, Harbin, China, where he delivered summer courses. He has authored more than 170 journal and conference articles, and holds several Spanish, European, and U.S. patents. His research interests include the implementation of complex control and processing algorithms and intelligent sensors in embedded platforms.

Prof. Rodríguez-Andina has coauthored the article awarded the 2017 IEEE Industrial Electronics Magazine Best Paper Award. He was also the recipient of the 2020 Anthony Hornfeck Award from the IEEE Industrial Electronics Society. From 2016 to 2021, he was the Vice President for Conference Activities of the IEEE Industrial Electronics Society. He was the Editor-in-Chief of the *IEEE Industrial Electronics Magazine* (2013–2015) and an Associate Editor for the IEEE TRANSACTIONS ON INDUSTRIAL ELECTRONICS (2008–2018). He is currently an Associate Editor for the IEEE TRANSACTIONS ON INDUSTRIAL INFORMATICS and the IEEE Open Journal of the Industrial Electronics Society.

WEICHAO SUN (Senior Member, IEEE) received the B.S. degree in automation from Central South University, Changsha, China, in 2007 and the M.S. and Ph.D. degrees in control science and engineering from the Harbin Institute of Technology, Harbin, China, in 2009 and 2013, respectively.

He is currently a Professor with the Research Institute of Intelligent Control Systems, Harbin Institute of Technology. His research interests include adaptive robust control, mechatronics, robotics, and autonomous vehicles.

Dr. Sun is currently an Associate Editor for IEEE TRANSACTIONS SYSTEMS, MAN, AND CYBERNETICS: SYSTEMS, MECHATRONICS and *Journal of Dynamic Systems, Measurement and Control*.

HUIJUN GAO (Fellow, IEEE) received the Ph.D. degree in control science and engineering from the Harbin Institute of Technology, Harbin, China, in 2005.

From 2005 to 2007, he was a Postdoctoral Researcher with the Department of Electrical and Computer Engineering, University of Alberta, Edmonton, AB, Canada. Since 2004, he has been with the Harbin Institute of Technology, where he is currently a Chair Professor and the Director of the Research Institute of Intelligent Control and Systems. His research interests include intelligent and robust control, robotics, mechatronics, and their engineering applications.

Dr. Gao is currently a Member of Academia Europaea and a Distinguished Lecturer of the IEEE Systems, Man and Cybernetics Society. He is also the Vice President of the IEEE Industrial Electronics Society and a Council Member of the International Federation of Automatic Control (IFAC). He is or was the Editor-in-Chief of the IEEE/ASME TRANSACTIONS ON MECHATRONICS, the Co-Editor-in-Chief of the IEEE TRANSACTIONS ON INDUSTRIAL ELECTRONICS, and an Associate Editor for the *Automatica*, IEEE TRANSACTIONS ON CYBERNETICS, and IEEE TRANSACTIONS ON INDUSTRIAL INFORMATICS.